 doi:10.20944/preprints202106.0411.v1

Article

Synthesis and Electrochemical Performance of Electrostatic Self-Assembled Nano-Silicon@N-Doped Reduced Graphene Oxide/Carbon Nanofibers Composite as Anode Material for Lithium-Ion Batteries

Ruye Cong[1], Hyun-Ho Park[1], Minsang Jo[2], Hochun Lee[2], Chang-Seop Lee[1,*]

[1] Department of Chemistry, Keimyung University, Daegu 42601, Korea

[2] Department of Energy Science and Engineering, DGIST, Daegu 42988, Korea

* Correspondence: surfkm@kmu.ac.kr; Tel.: +82-53-580-5192

Abstract: We report a self-assembly synthesis of silicon nanoparticles/nitrogen-doped reduced graphene oxide/ carbon nanofiber (Si@N-doped rGO/CNF) composites as potential high-performance anodes for rechargeable lithium-ion batteries (LIB) through the electrostatic attraction between amino and carboxyl groups. Nitrogen atoms generate a large number of vacancies or defects on the graphite plane, providing additional transmission channels for the diffusion of lithium ions, and improving the conductivity of the electrode. Carbon nanofiber (CNF) can help maintain the stability of the electrode structure and prevent silicon nanoparticles from falling off the electrode, prevent silicon nanoparticles from being directly exposed to the electrolyte, and can form a stable solid electrolyte interface (SEI) film. The three-dimensional conductive structure composed of Si, nitrogen atom-doped reduced graphene oxide (N-doped rGO), and CNF can effectively buffer the volume changes of silicon nanoparticles, shorten the transmission distance of lithium ions (Li^+) and electrons, and make the electrode have good conductivity and stability in mechanical properties. In addition, compared with the Si@N-doped rGO and Si/rGO/CNF composite electrode, the Si@N-doped rGO/CNF composite electrode shows good cycle performance and rate capability, and its reversible specific capacity can reach 1418.8 mAh/g. The capacity retention rate is 64.7%, and the coulomb efficiency is 95%.

Keywords: lithium-ion battery; silicon nanoparticles; nitrogen-doped graphene; carbon nanofibers; anode material

1. Introduction

Lithium-ion battery (LIB) has high energy density (its volume energy density and mass-energy density can reach 450 W.h/dm^3 and 150 W.h/kg respectively), high average output voltage (about 3.6 V), and large output power. With low self-discharge, wide operating temperature range (−30~+45°C), good environmental compatibility, and long cycle life, it is considered one of the most promising energy storage devices [1-3]. However, due to portable electronic equipment, computer equipment, sustainable or hybrid vehicles, and renewable energy storage stations, the demand for higher capacity and longer life batteries continues to grow with the progress of social development, which puts forward higher needs

Preprints (www.preprints.org) | NOT PEER-REVIEWED | Posted: 15 June 2021 doi:10.20944/preprints202106.0411.v1

for the performance of LIBs. Thus, scientists are committed to the development and research of high-performance electrode materials for LIBs [4-6].

Silicon (Si)-based materials are considered to be one of the most promising candidate materials for anode materials for LIB in the future. Because of its high theoretical specific capacity (~4,200 $mAhg^{-1}$), low lithiation potential (~0.4 V vs. Li/Li^+), rich natural content, low price, non-toxicity, and environmental safety, it is commonly used in lithium-ion anode material of the battery. However, the low conductivity of the active Si material leads to poor electrode rate performance, and the huge volume expansion (about 400%) of the silicon particles during the cycle will cause problems such as crushing of the electrode material and loss of electronic contact between the particles. This leads to reduced battery efficiency, shortened life cycle, and breakage of battery cells. In addition, the commonly used electrolyte will form a solid electrolyte interface (SEI) on the silicon surface at a potential of less than 1V. During the volume change, the SEI can crack and expose the exposed silicon particles, and more and more SEI is formed on the exposed silicon surface. The SEI film continuously increases the total layer thickness of the silicon particles and quickly fills the electrode holes, preventing the transmission of Li^+ and electrons, causing the battery capacity to rapidly decrease, thus limiting the practical application of LIBs in commerce [7-11].

To solve the above problems, silicon is combined with other materials (e.g., graphene, carbon nanotubes, carbon nanofibers, and other carbon materials) to obtain a composite material with a stable structure and buffer volume changes to improve conductivity and cycle stability. Graphene has excellent electronic conductivity, good physical and chemical stability, high thermal stability, excellent mechanical flexibility, and high theoretical surface area, as well as other unique structure and excellent performance. Therefore, it is recognized as an effective coating material for the preparation of lithium-ion batteries. The carbon-carbon bond length of graphene is 0.142 nm. The carrier mobility at room temperature is as high as 15,000 $cm^2\ V^{-1}\ s^{-1}$, and its corresponding resistivity is 10^{-6} Ωcm (the lowest resistivity among materials known in the art) [12-15]. Graphene-based silicon/carbon composite materials can not only improve the volume change of nano-silicon and form a stable SEI film but also improve the electrical conductivity and lithium storage performance of silicon nanoparticles. However, through research in previous experiments, it is found that the agglomeration of graphene particles itself may lead to the poor electrical conductivity of the electrode material, and may reduce the stability of the charge/discharge cycle process. Thus, graphene doped with nitrogen atoms has recently attracted great interest among scientists. Nitrogen atom-doped reduced graphene oxide (N-doped rGO) is considered to be effective in improving the physical and electrochemical properties of graphene. Because nitrogen atoms have two lone pairs of electrons and show more electronegativity than carbon atoms. Thus, the electron density of nitrogen-doped carbon becomes lower and has stronger electrochemical activity. The electronegativity of nitrogen is stronger than that of carbon, and the hybridization of the lone pair electrons of nitrogen and graphene π system forms p-π conjugation between the lone pair electrons of nitrogen and the π electrons of graphene in the plane of graphene, which can improve the charge-transfer capability of N-doped graphene, and increases conductivity. In addition, the nitrogen atoms will also create a large number of vacancies or defects on the graphite plane, thus

 doi:10.20944/preprints202106.0411.v1

providing additional transport channels for the wetting of the electrolyte and the diffusion of Li+. Therefore, N-doped graphene is considered to be a promising LiBs material [16-22]. According to previous reports, Xing Li et al. proposed that when the self-assembled encapsulation of Si in N-doped reduced graphene oxide is used as an anode material for lithium-ion batteries, which has the effect of improving electrochemical performance [23]. Ren Na et al. studied that the doping level of nitrogen is controlled by the amount of urea used in the reaction, and the thickness of the modified layer of Si is controlled by the time of aminopropyltriethoxylsilane (APTES) hydrolysis [24]. However, there are still problems that the diffusion distance of Li^+ through the interlayer channels of graphene increases with the superimposition of the electrode size, which reduces the lithium-ion storage performance of the graphene electrode. Then, due to the different volume expansion rates of silicon and graphene, Si nanoparticles are extremely likely to peel off from graphene after several charge/discharge cycles, resulting in a decrease in cycle performance.

Carbon nanofiber (CNF) has high heat capacity, chemical stability, high conductivity, good mechanical strength, and a large specific surface area. CNF wraps around the silicon particles, which can not only effectively accommodate and buffer the volume change of silicon but also prevent the electrode structure from cracking and prevent the silicon particles from falling off the carbon base due to the expansion of the surface area. In addition, the addition of carbon nanofibers can form a relatively robust three-dimensional (3D) structure, which can effectively increase the specific surface area and provide open channels for electrolyte immersion, reduce the stacking of graphene layers, and shortening the transmission distance of electrons and Li^+, it makes the electrode have good electrical conductivity and stable mechanical properties [25-29].

In this study, we designed a synthesis method of self-assembly by electrostatic attraction to prepare a self-supporting Si@N-doped rGO/CNF composite as an anode material, holding to the cost-saving and environment-friendly design concept, achieving a stable cycle of electrochemical materials, and obtaining a LIB anode material with excellent mechanical flexibility and lightweight. First, the surface of Si nanoparticles was modified with piranha solution, and Si@APTES was formed by the positive charge from the hydrolysis reaction of APTES. This creates a condition for SiNPs to be highly diffuse in an aqueous system, which is conducive to improving the bonding force between Si and rGO. Second, using urea as a precursor, nitrogen atoms are incorporated into the plane of graphene through a hydrothermal reaction. The level of nitrogen doping is controlled by the amount of urea used in the reaction. Then, the sponge-like N-doped GO, CNF, and modified SiNPs were combined to prepare Si@N-doped GO/CNF composites by a simple physical mixing method. Finally, Si@N-doped rGO/CNF was obtained by annealing the Si@N-doped GO/CNF mixture in an argon atmosphere. In the obtained structure, the sponge-like flexible N-doped rGO, CNF, and silicon nanoparticles (SiNPs) work together to establish a continuous conductive network, which provides an effective channel for the diffusion of Li^+, which is expected to improve the cycle stability of the nanocomposite and rate performance.

2. Experimental

2.1. Materials and Chemicals

Preprints (www.preprints.org) | NOT PEER-REVIEWED | Posted: 15 June 2021 doi:10.20944/preprints202106.0411.v1

Iron (III) nitrate nonahydrate ($Fe(NO_3)_3 \cdot 9H_2O$, 98%), copper (II) nitrate trihydrate ($Cu(NO_3)_2 \cdot 3H_2O$, 99%), aluminum nitrate ($Al(NO_3)_3 \cdot 9H_2O$), molybdate ($(NH_4)_6Mo_7O_{24} \cdot 4H_2O$), ammonium carbonate ($(NH_4)_2CO_3$), hydrogen peroxide ($H_2O_2$, 30%) and urea ($CH_4N_2O$, ≥98%) were purchased from Daejung Chemicals & Metals CO in Korea. All the reagents were of analytical grade and used as received. Silicon nanoparticles (powder, APS≤50 nm, 98%) were purchased from Alfa Aesar, Inc. Graphene oxide (GO) was purchased from Angstron materials (Dayton, OH, U.S.A N002-PS, 0.5%) and used as received. (3-aminopropyl) triethoxysilane (APTES, ≥99%) was provided from AcroSeal in Korea. Ethyl alcohol (anhydrous, 99.9%) and sulfuric acid (H_2SO_4, 95–98%) were purchased from Sigma-Aldrich. Deionized (DI) water was used for preparing all the aqueous solutions throughout the experiments.

2.2. Synthesis of Si@APTES and CNF

First, the SiNPs were immersed in a solution of piranha (H_2SO_4/H_2O_2=3:1 v/v) to introduce hydroxyl groups on the surface. 30 ml of sulfuric acid solution was added to the beaker, then slowly 10 ml of the hydrogen peroxide solution was added to the beaker containing the sulfuric acid solution, and the two were thoroughly mixed while stirring to form a homogeneous solution of piranha. Then, 0.2 g of SiNPs were added to the piranha solution, and stirring was continued for 8 h in a water bath at 80°C. After that, the mixture solution was vacuum filtered and washed with deionized water several times to remove the excess piranha solution on the surface of the SiNPs. Then, the pre-treated SiNPs were dried in a vacuum oven at 60°C for 24 h. Second, the dried SiNPs were diffused in 400 ml of DI water, and 8 ml of APTES was added to the solution, and stirring was continued for 24 h. Finally, the obtained SiNPs@APTES solution was washed several times with DI water to remove excess APTES and then placed in a vacuum oven at 60°C for 24 h.

We used co-precipitation to prepare a bimetallic Fe–Cu (70:30 at.%) catalyst for the synthesis of carbon nanofibers. The Fe–Cu catalyst was used to synthesize carbon nanofibers by chemical vapor deposition (CVD). The synthesis process is shown in Supplementary Figure S1[30].

2.3. Synthesis of Si@N-doped rGO/CNF and Si@N-doped rGO

We added 2 g urea (CH_4N_2O) to 40 ml GO (0.5%) solution and mixed for about 12 h until completely dissolved. The prepared Si@APTES and GO solution were thoroughly mixed and diffused in the ethanol aqueous solution, and ultrasonic grinding was performed for 4 h. Then, the previously mentioned CNF (0.2 g) was added, and the mixture was ultrasonically milled again for 4 h, and continuously stirred for 4 h, so that the substances were fully mixed through physical processes to obtain a highly stable Si@N-doped GO/CNF complex. Thus, the homogeneous solution was transferred into a Teflon-lined stainless-steel autoclave and remained at 180°C for 24 h. Then, vacuum filter the prepared Si@N-doped GO/CNF diffusion and washed with DI water, and dried the filtered composite in an incubator at 60°C for 24 h, and then peel the composite from the filter paper to obtain the Si@N-doped GO/CNF composite membrane. Finally, the obtained Si@N-doped GO/CNF composite film was heated to 700°C at a rate of 10°C/min in a quartz tube furnace with argon (Ar) gas flow and kept for 5 h to obtain a thermally reduced Si@N-doped rGO/CNF composite material.

Preprints (www.preprints.org) | NOT PEER-REVIEWED | Posted: 15 June 2021 doi:10.20944/preprints202106.0411.v1

To compare the electrochemical performance, another Si@N-doped rGO composite membrane electrode without CNF was prepared by the same method as a control sample. The entire material preparation process is shown in Figure 1.

2.4. *Materials characterization*

The surface morphology and microstructure of the Si@N-doped rGO/CNF and Si@N-doped rGO composite was characterized by field-emission scanning electron microscopy (SEM, Hitachi S-4800) and high-resolution transmission electron microscopy (HRTEM, JEM-2100). The qualitative and quantitative analysis of the elements of the prepared samples was performed by energy-dispersive X-ray spectroscopy (EDX, Thermo ARL, ARL-3460). The characterizations of the sample composition and crystal structure were performed by taking power X-ray diffraction (XRD) measurements using an Ultima IV, 2 kW system with Cu-Kα radiation (K=1.5418 Å), scanned with the 2θ range from 2° to 90°. Raman spectroscopy analysis was performed on a Horiba Jobin-Yvon (Raman, LABRAM HR-800) with a laser light (λ=514 nm) in a wavenumber range of 100–3000 cm^{-1}. Fourier transform infrared spectroscopy (FTIR) of the sample was performed with KBr pellet in the frequency range of 4000–500cm^{-1} from the Nicolet 6700 spectrophotometer. X-ray photoelectron spectroscopy (XPS, Thermo Fisher Scientific, Multilab-2000) analysis was performed on a twin anode with Al Kα radiation as an X-ray source. The amounts of SiNPs, N-doped rGO, and CNFs in the composites were measured by thermogravimetric analysis (TGA) using the Perkin Elmer Diamond TG/DAT thermal analyzer, from 25 ℃ to 800 ℃ at a heating rate of 10℃/min under an atmosphere.

2.5. *Fabrication of LIBs and Electrochemical measurements*

In this study, two-electrode batteries were prepared using Si@N-doped rGO/CNF and Si@N-doped rGO composite materials as active anode materials for LIBs. To test the electrodes and characterize their electrochemical performances, the working electrodes were prepared by mixing 80 wt% active material, 10 wt% Super P carbon black (conductive agent), and 10 wt% polyvinylidene fluoride (PVDF) binder. The mixture was dissolved in an appropriate amount of N-methylpyrrolidinone (NMP) solvent, which was poured to prepare a mixture of uniformly dispersed negative electrode active slurry. The slurry was coated on the copper foil current collector and dried at 80 ℃ for 24 h under a vacuum to form the electrode plate. The electrodes were punched into a negative pole disk with a diameter of 14 mm and the average load density of each electrode was about 1 mg/cm^2. Metallic lithium foil as the counter and reference electrodes, and two-electrode lithium-ion coin cells (CR2032) were assembled in a high-purity argon-filled glove box. The separator membrane was Celgard 2600, and the electrolyte was a solution of 1 M $LiPF_6$ dissolved in a mixture of ethylene carbonate (EC)/dimethyl carbonate (DMC)/ethyl methyl carbonate (EMC) (1:1:1 by volume). The coin cells galvanostatic charge-discharge measurements were tested at the voltage range of 0.01–1.5 V (vs.Li/Li^+) using a battery tester (Neware Co., Ltd. Shenzhen, China). The specific capacity is calculated based on the whole mass of the anode material. The cyclic voltammetry (CV) was performed with a scan rate of 0.5 $mV{\cdot}s^{-1}$ between the voltage range of 0.01–1.5 V, at room temperature (25℃). Electrochemical impedance spectroscopy (EIS) measurements were taken on a CHI 660D electrochemical analysis instrument (CH Instruments, Inc. Shanghai,

 doi:10.20944/preprints202106.0411.v1

China) between the frequency ranging from 100 kHz to 10 mHz with an amplitude of 5 mV.

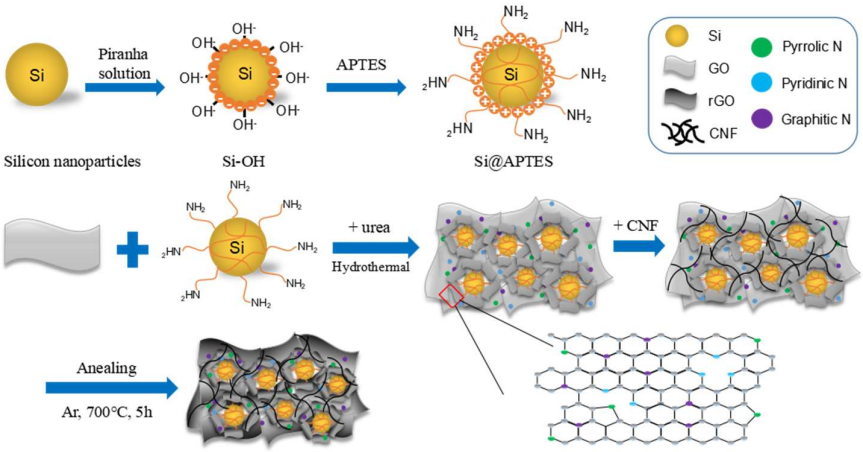

Figure 1. Schematic diagram of the preparation process of Si/N-doped rGO/CNF and Si/N-doped rGO composite material.

3. Results and discussion

3.1. Structure and morphology

Figure 1 shows the schematic preparation process of Si@N-doped rGO/CNF composite material. First, the Si nanoparticles are diffused in the piranha solution. This process can modify the surface of the Si nanoparticles, that is, the hydroxyl groups are grafted on the surface of the Si nanoparticles to form Si-OH. Second, after adding APTES to it and going through the hydrolysis process of APTES, the siloxane group of APTES is easily grafted onto the Si nanoparticles with–OH end caps [31-33]. Then, the APTES functionalized Si nanoparticles were directly diffused in the urea-dissolved GO hydrosol by ultrasonic treatment, and CNF was added thereto. During the hydrothermal process, amino groups (−NH2) on the surface of APTES functionalized Si nanoparticles can easily bond with the epoxy and carboxyl groups on the GO surface, causing electrostatic interactions. At the same time, during the decomposition of urea, a large number of N atoms can be introduced into the planar structure of GO to form different types of N-doped GO configurations. Finally, the Si@N-doped rGO/CNF composite was obtained by calcination at high-temperature under an argon atmosphere. This design process not only ensures that Si nanoparticles can be uniformly diffused in the network formed by rGO, but the introduction of CNF also prevents Si nanoparticles from falling off the graphene sheet, effectively buffering the volume change of Si nanoparticles. In addition, N-doped rGO is also beneficial to improve the conduction of electrons and the diffusion of Li^+ and improve the conductivity of the electrode [23, 24, 34].

The SEM images of Si@N-doped rGO/CNF and Si@N-doped rGO composites are shown in Figure 2. Figure 2(a–c) shows that the surface of the graphene nanosheets is anchored with a large number of Si nanoparticles, and these Si nanoparticles are not seriously agglomerated but are evenly distributed on the graphene sheets. However, for Si@N-doped rGO/CNF composites, we observed different morphologies (Figure 2(d–f)). The Si nanoparticles wrapped in the graphene sheet are tightly entangled by the carbon nanofibers, and the carbon

Preprints (www.preprints.org) | NOT PEER-REVIEWED | Posted: 15 June 2021 doi:10.20944/preprints202106.0411.v1

nanofibers are interspersed between the Si nanoparticles to form a stable 3D structure. The well-spaced structure can effectively adapt to the volume change of the entire electrode structure, reducing electrode pulverization and providing the electrode with excellent mechanical integrity. In addition, the Si nanoparticles are tightly wrapped by wrinkled graphene sheets, which may be due to the introduction of a large number of defects in rGO due to the doping of nitrogen atoms, creating more binding sites. And it is the result of a close combination with Si nanoparticles after surface modification. Such an electrode structure will undoubtedly improve its electrochemical performance.

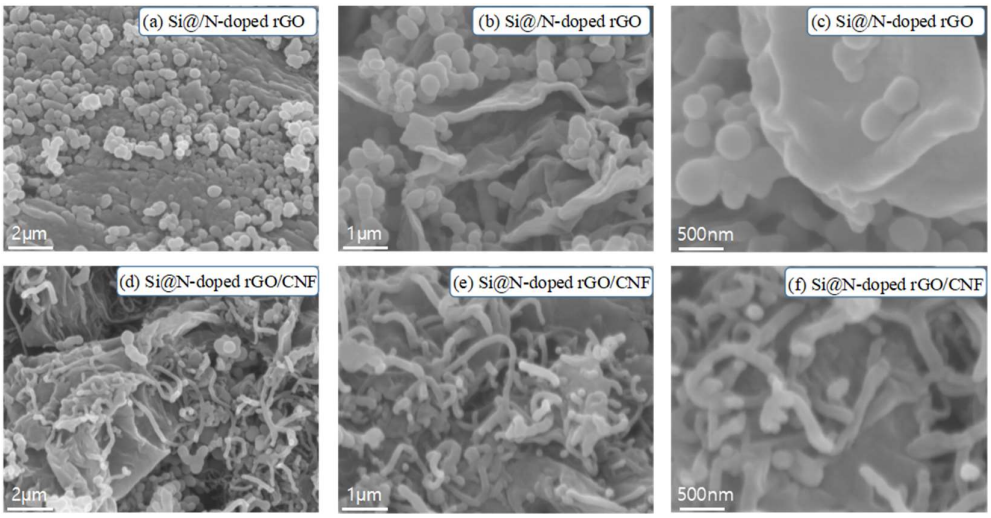

Figure 2. SEM images of the Si@N-doped rGO (a–c) and Si@N-doped rGO/CNF (d–f) composites.

To study the structure and morphology of the composite material more clearly and in detail, we performed a transmission electron microscope (TEM) image analysis of the composite material (Figure 3). Figure 3(a, b) shows the TEM image results of the Si@N-doped rGO composite. We can observe that the Si nanoparticles are uniformly diffused on the wrinkled graphene sheet without serious agglomeration. This is consistent with the expected results. Second, the Si@N-doped rGO/CNF composites were introduced into CNF (Figure 3(c, d)); graphene-encapsulated Si nanoparticles are distributed in the cross-linked CNF grid and are tightly entangled by CNF. And graphene and CNF form a woven structure together. This effectively prevents Si nanoparticles from falling off the graphene sheet due to volume changes and helps maintain the original electrode structure. This is consistent with the results of the SEM images. In addition, Figure 3(e) shows that the interplanar spacing of Si nanoparticles is 0.315 nm, and the obvious fringes are identified as Si (111) planes. In Figure 3(f), the bright diffraction spots in the three diffraction rings of the selected area electron diffraction (SAED) correspond to the (111), (220), and (311) crystal planes of the Si nanoparticles [35]. At the same time, we give an analysis of the EDX spectrum results of the Si@N-doped rGO/CNF composite in the supplementary material (Figure S2). As shown in the mapping image, in addition to the Si element, we also detected the C, N, and O elements in the sample. This mainly comes from N-doped rGO and CNF. This shows that N atoms were successfully doped into rGO and tightly

Preprints (www.preprints.org) | NOT PEER-REVIEWED | Posted: 15 June 2021 doi:10.20944/preprints202106.0411.v1

combined with the modified Si nanoparticles. This effectively prevents the direct contact between the exposed Si nanoparticles and the electrolyte to produce a thicker SEI layer, and the flexible graphene which can effectively buffer the volume change of the Si nanoparticles in the charging and discharging process, thus improving the electrochemical performance of the composite material.

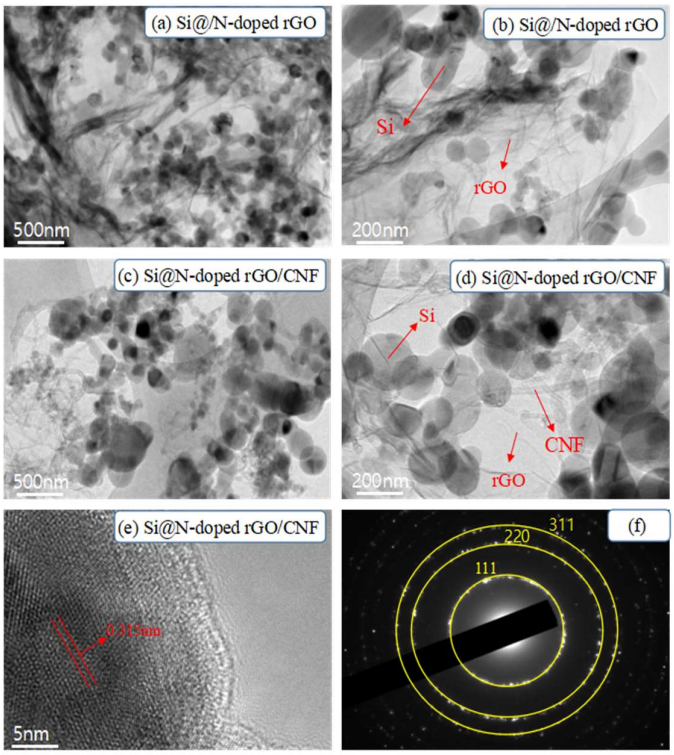

Figure 3. TEM images of Si@N-doped rGO (a,b), Si@N-doped rGO/CNF (c,d) composites, (e) High-resolution TEM images of Si@N-doped rGO/CNF composites, (f) Selected Area Electron Diffraction (SAED) pattern of Si.

The X-ray diffraction (XRD) pattern in Figure 4 shows the crystal structure characteristics of GO, rGO, CNF, Si, Si@N-doped rGO, and Si@N-doped rGO/CNF. Si, Si@N-doped rGO, and Si@N-doped rGO/CNF have the same characteristic peaks at 28.4°, 47.3°, and 56.0°, respectively, corresponding to Si (111), (220) and (311) crystal surface (JCPDS 27–1402) [36]. This result is consistent with the results of SAED and shows that Si successfully exists in the composite material, and there is no structural change in Si during the process of synthesizing the composite material. In addition, in GO, a strong and narrow representative diffraction peak appears at 2θ=9.8°, which corresponds to the lattice plane of GO (002). In the curve of rGO, the characteristic peaks of GO at 9.8° and around 20° disappeared, but a new peak appeared near 25°, showing that GO was successfully reduced to rGO in an argon atmosphere at 700 °C [37]. In the Si@N-doped rGO and Si@N-doped rGO/CNF composites, the characteristic peak of rGO also appears near 25°, and its lower strength can be attributed to the relatively higher strength of Si. In addition, there are no other new peaks in the Si@N-doped rGO composite, which shows that no other impurities were introduced in the process of self-assembly and nitrogen doping. At the same time, there is also a weak peak

Preprints (www.preprints.org) | NOT PEER-REVIEWED | Posted: 15 June 2021 doi:10.20944/preprints202106.0411.v1

near 44° of the Si@N-doped rGO/CNF composite, which corresponds to the characteristic peak of CNF.

To further study the microstructure of amorphous carbon, GO, rGO, CNF, Si@APTES/N-doped GO, Si/rGO, Si@N-doped rGO, and Si@N-doped rGO/CNF were Raman scattering, the spectrum result is shown in Figure 4b. It can be seen that, except for GO and rGO samples, the same characteristic peaks near 515 and 956 cm^{-1} are detected in all other samples, which corresponds to the typical Raman mode of crystalline Si [38]. It was further confirmed that the silicon crystal did not change during the process of preparing the composite material and had good crystallinity. In addition, for all samples, two peaks were detected at 1348 cm^{-1} (D band) and 1580 cm^{-1} (G band). Among them, the D band is related to the structural defects and disordered structure in the hexagonal graphite, corresponding to sp3 hybridized disordered carbon; while the G band corresponds to the well-defined sp2 hybridized ordered carbon in the graphite sheet. The relative peak intensity ratio (ID/IG) of the D band and the G band can be used as an important indicator for evaluating the degree of graphitization of carbonaceous materials and the defect density in graphene-based materials. The lower the ID/IG value, the higher the degree of graphitization, and the better the conductivity [23, 39]. The ID/IG ratios of samples GO, rGO, CNF, Si@APTES/N-doped GO, Si/rGO, Si@N-doped rGO, and Si@N-doped rGO/CNF are 1.05, 0.96, 0.99, 1.03, 1.02, 1.00, and 1.00, respectively (Supplementary Table S1). This shows that the Si@N-doped rGO and Si@N-doped rGO/CNF samples have the highest degree of graphitization and therefore have the best electrical conductivity. After heat treatment and reduction, the ID/IG value of Si@N-doped rGO is smaller than that of Si@APTES/N-doped GO. This is because most of the oxygen groups removed from the graphene nanosheets and the graphitic carbon structure are reconstructed, which leads to an increase in the disorder of Si@N-doped rGO, and as the degree of carbonization increases, the size of the area in the sp2 plane in the plane increases, while the strength of the D band decreases. Comparative samples Si/rGO and Si@N-doped rGO, due to the introduction of N atoms in the graphitic carbon structure, the defects of graphitic carbon increase, therefore, the ID/IG value of Si@N-doped rGO is smaller than the ID/IG value of Si/rGO [40]. In addition, because CNF itself has some defects, adding CNF will weaken the D band, resulting in a reduction in the ID/IG value. These defects can provide more abundant channels for the transportation of Li^+, reduce the resistance of lithium-ion migration, and improve the electrochemical performance of the composite material [41].

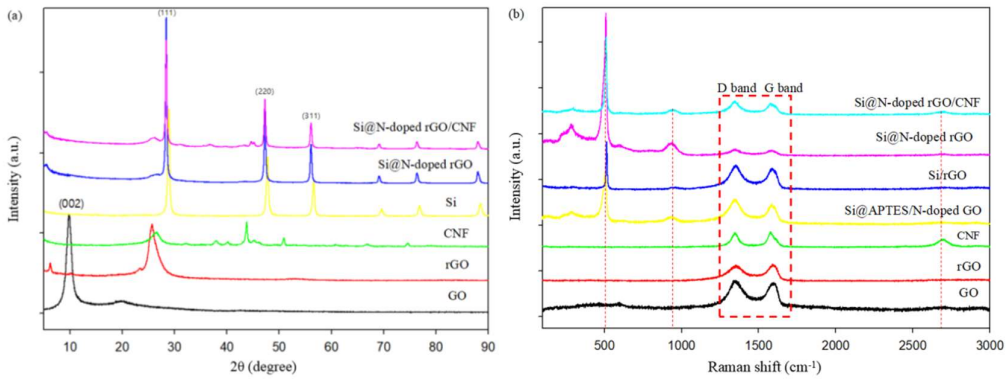

 doi:10.20944/preprints202106.0411.v1

Figure 4. (a) X-ray diffraction patterns of GO, rGO, CNF, Si, Si@N-doped rGO and Si@N-doped rGO/CNF, (b) Raman spectra of the GO, rGO, CNF, Si@APTES/N-doped GO, Si/rGO, Si@N-doped rGO, and Si@N-doped rGO/CNF.

By using XPS to compare Si-OH, Si@APTES, Si@APTES/N-doped GO, Si@APTES/N-doped GO/CNF, Si@N-doped rGO, and Si@N-doped rGO/CNF samples, the surface composition and the chemical state of each element are characterized (Figure 5). Figure 5(a) shows the obtained whole XPS spectra of Si@APTES, Si@APTES/N-doped GO, Si@APTES/N-doped GO/CNF, Si@N-doped rGO, and Si@N-doped rGO/CNF samples. Si, C, O, and N elements were detected in the sample. Figure 5(b) shows the high-resolution spectra of Si 2p for each sample. There are two distinct peaks at 99.5 and 103.2 eV, which are attributed to bulk silicon (Si-Si) and silicon-bonded to oxygen (Si-O), respectively. This shows that in the process of material preparation, a small amount of nano-scale silicon powder is exposed to the air and the surface is oxidized at a certain temperature to produce a small amount of SiO_2. By comparing the Si 2p spectra of Si@APTES and Si-OH, it is easy to find that the Si-O peak (103.2 eV) has increased, which is attributed to two factors. First, APTES itself contains many Si-O bonds. Second, the surface of the bulk silicon is covered by APTES, which results in the attenuation of the XPS signal of the bulk Si due to the limited probe depth of XPS. In addition, compared with the Si 2p spectra of Si@APTES, it can be seen that the Si-O peaks in the Si 2p spectra of Si@APTES/N-doped GO and Si@APTES/N-doped GO/CNF are significantly increased. This is due to the introduction of GO. As shown in Figure 5(c), there are three peaks in the C 1s of the Si-OH and Si@APTES samples, which represent the C-C at 284.5eV, C-O/C-N at 286.5eV, and O-C=O at 288.9 eV. After adding GO and CNF, a new peak appeared in the C 1s of Si@APTES/N-doped GO/CNF and Si@N-doped rGO/CNF, which represent C=O at 287.7 eV. It can be seen that compared with Si@APTES/N-doped GO/CNF, the intensity of the C-C peak in the C 1s of the reduced Si@N-doped rGO/CNF is improved, the intensity of the C-O/C-N, O-C=O, and C=O peak is reduced. This is the result of oxygen loss after thermal reduction. The N 1s spectra of Si@APTES and Si@N-doped rGO/CNF are shown in Figure 5(d). Two prominent peaks of 399.0 and 402.5 eV can be observed in the spectrum of Si@APTES, corresponding to the strong hydrogen bonds of amides–NH2 and free–NH2. Three diffraction peaks at 398.5, 400.6, and 403.9eV can be observed in the spectrum of Si@N-doped rGO/CNF. This is the characteristic peak of pyridine N, pyrrole N, and graphite N. Thus, the content of pyridine N is slightly higher than that of pyrrole N. Pyridine N and pyrrole N may be attributed to the substitution of N atoms for C atoms at the edges or defects of graphene, thereby providing additional channels for lithium-ion diffusion. Graphite N forms a C-N covalent bond by replacing the internal C atoms with N atoms, which is advantageous for improving the conductivity of the graphene sheet.

Preprints (www.preprints.org) | NOT PEER-REVIEWED | Posted: 15 June 2021 doi:10.20944/preprints202106.0411.v1

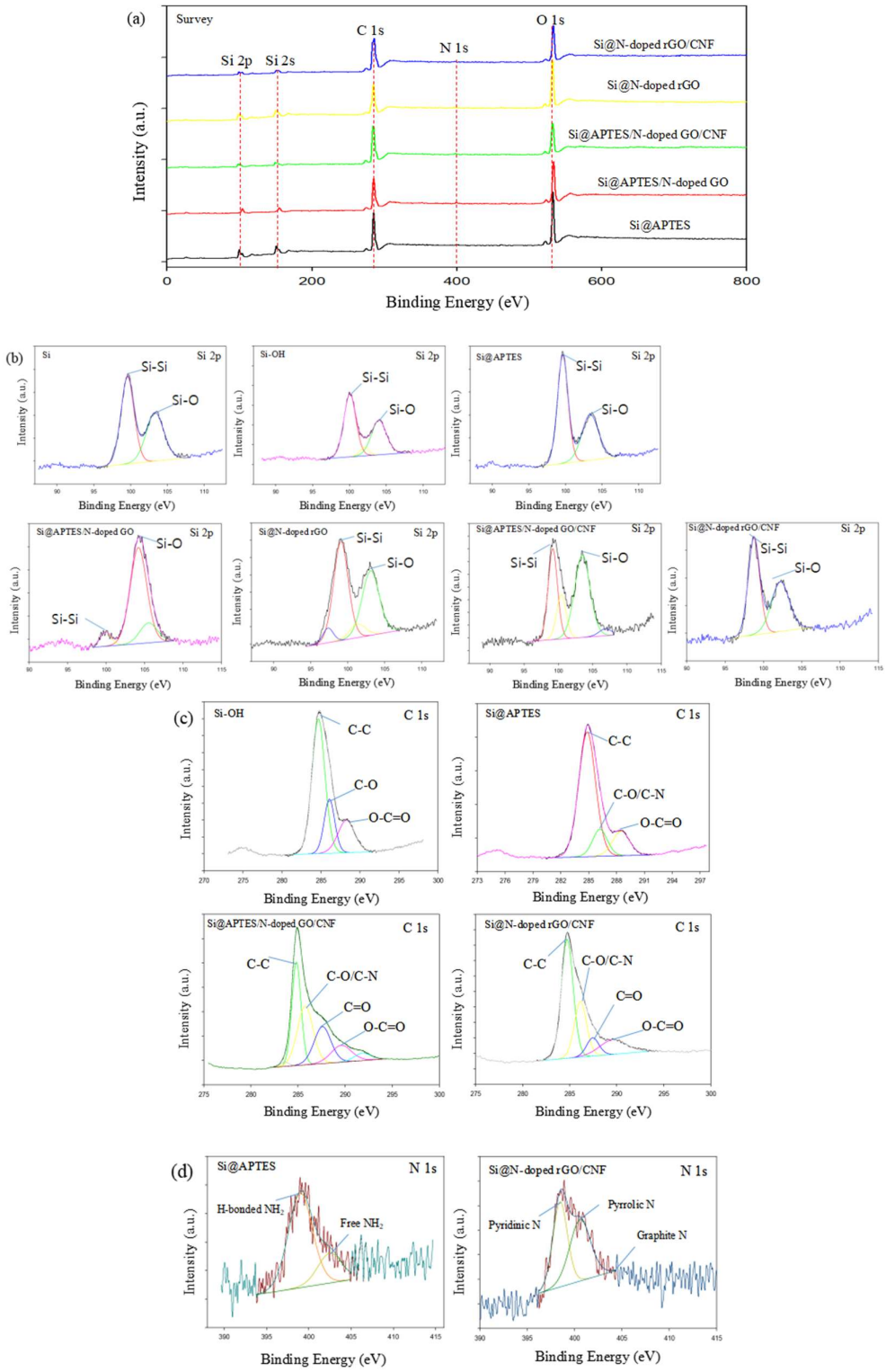

Figure 5. (a) Survey XPS spectra of Si@APTES, Si@APTES/N-doped GO, Si@APTES/N-doped GO/CNF, Si@N-doped rGO, and Si@N-doped rGO/CNF, (b) Si 2p XPS spectra of Si, Si-OH, Si@APTES, Si@APTES/N-doped GO, Si@APTES/N-doped GO/CNF, Si@N-doped rGO and Si@N-doped rGO/CNF, (c) C 1s XPS spectra of Si-OH, Si@APTES, Si@APTES/N-doped GO/CNF and Si@N-doped rGO/CNF, (d) N 1s XPS spectra of Si@APTES and Si@N-doped rGO/CNF.

 doi:10.20944/preprints202106.0411.v1

The surface chemical structure of the relevant sample is shown in the FTIR spectrum (Figure 6). In Figure 6a, the three samples all have strong absorption peaks between 1200 and 1000 cm^{-1}, which corresponds to the asymmetric stretching and bending of the siloxane group (Si-O-Si) [24]. For pure Si nanoparticles, this is because the surface of Si nanoparticles is oxidized by air to produce a small amount of SiO_2. This is consistent with the results of XPS. Between 1800 and 1600 cm^{-1}, there is an absorption peak in each of the three samples, which corresponds to the vibration of H_2O molecules. It is easy to find that the vibration of H_2O molecules in Si-OH is stronger, which shows that due to the presence of hydrophilic–OH groups and more H_2O molecules are easily adsorbed on the surface of Si-OH [23, 44]. In the Si@APTES sample, there is an absorption peak at 2930 cm^{-1}, which is attributed to the vibration of methyl/methylene (-CH2-) in the APTES molecule. After reduction by heat treatment, the peak disappeared. Thus, the broad peaks between 3100 and 3500 cm^{-1} are attributed to some hydrogen bond interactions between the–NH2 groups in APTES and the hydroxyl groups (–OH) on the surface of the Si nanoparticles [43-44]. These observations show that the surface of Si nanoparticles is rich in amino groups. In addition, we found that the Si-OH spectrum has an obvious characteristic absorption peak at 3480 cm^{-1}, which is attributed to the vibration of the–OH bond, and the peak at 3760 cm^{-1} is much stronger than the peak in the Si@APTES spectrum. We can conclude that APTES has been successfully grafted onto Si-OH.

For the FTIR spectrum of GO (Figure 6b), the absorption peaks at 1715 and 1078 cm^{-1} are attributed to the stretching vibration of the -C=O bond in -COOH and the -C-O bond in -C-OH, respectively. By comparing the spectra of GO with the other two samples, it can be observed that the relative intensity of the absorption peak at 1715 cm^{-1} in Si@APTES/N-doped GO and Si@APTES/N-doped GO/CNF samples is significantly improved, and the peak at 1645 cm^{-1} disappeared, which was attributed to the stretching vibration of the -C=O bond and -C=N bond of the amide [45-48]. Based on the above analysis, we can conclude that a chemical cross-linking reaction with strong hydrogen bond interaction occurred between Si @ APTES and GO.

Figure 6c shows the thermogravimetric analysis curves (TGA) of Si@N-doped rGO/CNF, Si@N-doped rGO, and pure nano-Si in an air atmosphere. In the TGA curve, the weight of the Si@N-doped rGO/CNF composite sample decreased rapidly between 400 °C and 560 °C. This is due to the degradation and rapid oxidation of rGO and CNF. It can be inferred from the result that the weight of the Si@N-doped rGO sample drops rapidly after 550 °C. In the TGA curve of Si@N-doped rGO/CNF samples, CNF is the first to decompose between 400 °C and 440 °C. However, the weight of pure nano-Si and composite materials significantly increased after 580 °C. This is due to the difficulty of oxidation of the inside of Si nanoparticles and the formation of a small amount of SiO_2 on the surface [40, 41, 49, 50]. This is consistent with the results of XPS and FTIR. Therefore, the weight loss of Si@N-doped rGO/CNF and Si@N-doped rGO samples can be calculated. In the Si@N-doped rGO/CNF sample, the content of N-doped rGO is 13.2%, the content of CNF is 33.4%, and the content of Si nanoparticles is 53.4%. In the Si@N-doped rGO sample, the content of N-doped rGO is 32.3%, and the content of Si nanoparticles is 67.7%.

Preprints (www.preprints.org) | NOT PEER-REVIEWED | Posted: 15 June 2021 doi:10.20944/preprints202106.0411.v1

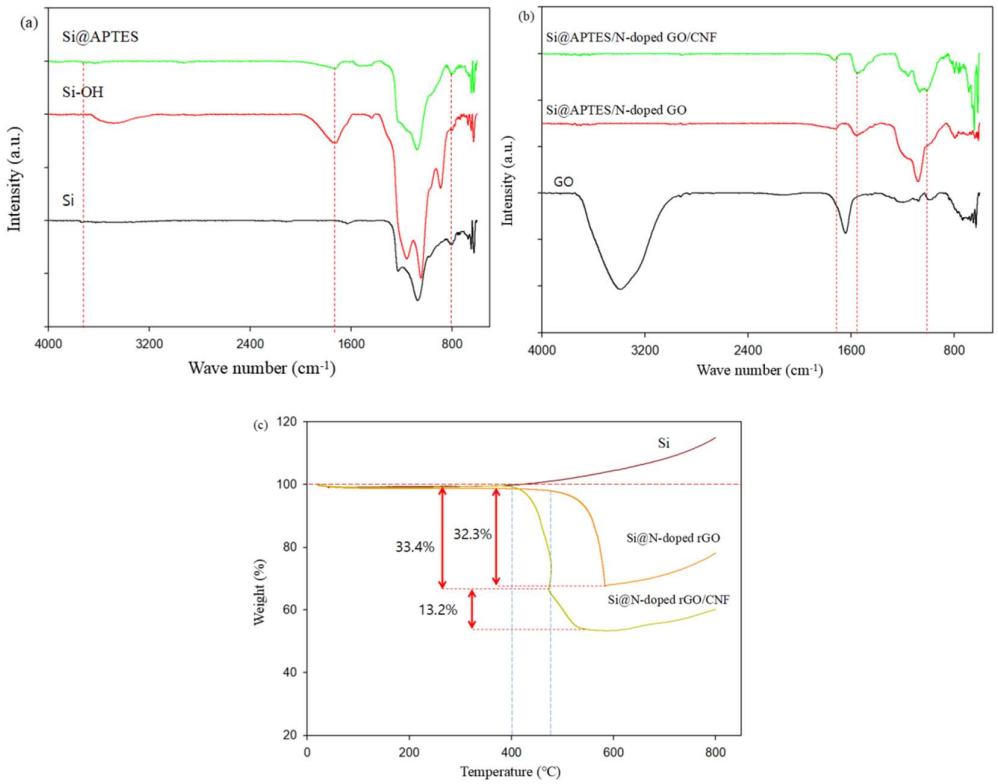

Figure 6. (a) Fourier transforms infrared (FTIR) spectra of Si, Si@OH and Si@APTES, (b) Fourier transform infrared (FTIR) spectra of GO and Si@APTES/N-doped GO and Si@APTES/N-doped GO/CNF, (c) TGA curves of the pure nano-Si, Si@N-doped rGO, and Si@N-doped rGO/CNF composite material.

3.2. *Electrochemical performance*

Figures 7(a) and 7(b) show the cyclic voltammetry (CV) curves of the coin cell made of Si@N-doped rGO and Si@N-doped rGO/CNF electrodes during the first 5 cycles, within the potential voltage window of 0.01–1.5 V (vs Li^+/Li) at a scan rate of 0.1 mVs^{-1}. It can be seen that the CV curve of the first cycle of the two electrodes is different from the other subsequent cycle curves. In the first cycle of cathodic scanning, a broad and weak cathodic peak appeared near 1.10–1.40 V, which may be related to the reaction between the electrode material and the electrolyte and the formation of an irreversible SEI film on the electrode surface. However, the cathode peak disappeared in the subsequent cycles, showing that a stable SEI film was formed on the surface of the electrode material after the first cycle [22, 23, 24]. In addition, the cathode of Si@N-doped rGO/CNF is stronger than Si@N-doped rGO at 1.10–1.40 V. This is because the materials introduced with CNF have many defects, which contribute to the electrochemical reaction between the electrode and electrolyte. The strong reduction peak around 0.01–1.2 V corresponds to the amorphous LixSi alloy formed by amorphous silicon during the reversible lithium-ion intercalation/deintercalation process. During the delithiation process, the two oxidation peaks at 0.35–0.37V and 0.52–0.55 V are attributed to the extraction of Li^+ from the lithium-silicon alloy, and the LixSi alloy decomposes into amorphous silicon [34, 49]. In addition, as the number of scans increases, the intensity of the anode peak also gradually increases. This is because the composite electrode material is gradually activated during the cycle, showing

Preprints (www.preprints.org) | NOT PEER-REVIEWED | Posted: 15 June 2021 doi:10.20944/preprints202106.0411.v1

that more lithium tends to alloy with Si. This is consistent with previous reports [40,42,50].

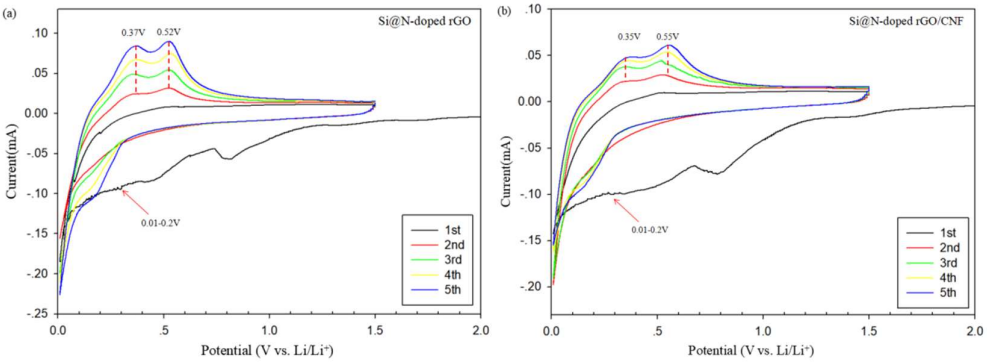

Figure 7. Cyclic voltammetry curves of the synthesized Si@N-doped rGO (a) and Si@N-doped rGO/CNF (b) electrodes in the initial five cycles.

The cycle performance comparison of each sample at a current density of 100 mAg^{-1} is shown in Figure 8(a). The charge and discharge capacity value, coulomb efficiency, and capacity retention rate of each sample are listed in Supplementary Table S2. Although both Si@N-doped rGO and Si/rGO/CNF composites have higher initial capacities, 3138.8 and 3434.9 mAh/g, respectively, after the first cycle, the capacity is extremely attenuated, which may be attributed to the electrode cannot adapt to the change in the volume of silicon particles during the lithiation/delithiation process, an SEI layer is formed on the surface of the electrode after contact with the electrolyte. However, compared with Si@N-doped rGO and Si/rGO/CNF composite electrodes, Si@N-doped rGO/CNF electrodes show better cycle performance. The initial discharge capacity was 2192.3 mAh/g. After 30 cycles, the capacity retention rate was 64.7% (1418.8 mAh/g). The coulomb efficiency is as high as 95% (Figure 8(c)). The capacity of the Si@N-doped rGO electrode remains at 1093.1 mAh/g after 89 cycles, and the capacity retention rate is 34.8%. The capacity of the Si/rGO/CNF electrode remained at 989.5 mAh/g after 89 cycles, and the capacity retention rate was only 28.9%. The excellent cycle performance of the Si@N-doped rGO/CNF electrode is not only attributed to the surface modification of silicon nanoparticles to improve the bonding ability between N-doped graphene and silicon nanoparticles but also the introduction of CNF prevents the silicon nanoparticles fall off the surface of graphene due to the volume change. The close contact between CNF and graphene and silicon nanoparticles constitutes a 3D cross-linked structure, which can buffer the volume expansion of silicon nanoparticles and effectively suppress the pulsation of silicon nanoparticles caused by huge volume changes. In addition, the presence of many vacancies and defects in N-doped graphene introduces more reaction sites, and N atoms increase the storage capacity of reversible Li^+, which improves the conductivity of the electrode material. In addition, the modified silicon nanoparticles can be uniformly distributed on the N-doped graphene sheet, preventing the aggregation and accumulation of silicon nanoparticles. This provides more effective channels for the conduction of ions and electrons and promotes the transfer of ions and electrons.

 doi:10.20944/preprints202106.0411.v1

To further illustrate the electrochemical performance of the Si@N-doped rGO/CNF electrode, figure 8(b) shows the rate performance of Si@N-doped rGO and Si@N-doped rGO/CNF electrode under the current density range of 0.1A/g–1A/g. Compared with the capacity of the Si@N-doped rGO electrode, the Si@N-doped rGO/CNF electrode exhibits a higher capacity at each current density. Si@N-doped rGO electrode is at 0.1, 0.2, 0.5, 1, 0.5, 0.2, and 0.1 A/g current density, after 10 cycles shows 1368.0, 1233.7, 1170.6, 1137.4, 1180.1, 1218.8, and 1261.8 mAh/g, respectively. However, the Si@N-doped rGO/CNF electrode has a current density of 0.1, 0.2, 0.5, 1, 0.5, and 0.2 A/g, after 10 cycles shows 1504.0, 1466.2, 1415.7, 1363.0, 1393.9, and 1414.1 mAh/g, respectively. When the current density returns to 0.1 A/g again, the reversible capacity can be maintained at 1433.9 mAh/g. The low specific capacity may be due to the Si nanoparticles being peeled from the graphene sheet due to the shrinkage/expansion of their volume during the charge/discharge process, resulting in direct contact between the Si nanoparticles and the electrolyte solution to form a thicker SEI film. In addition, the diffusion distance of Li+ through the channels between graphene layers will also increase with the superposition of the electrode size, thereby reducing the lithium-ion storage performance of the graphene electrode and affecting the electrochemical performance. On the contrary, the excellent rate capability of the Si@N-doped rGO/CNF electrode may be related to the good conductivity of the graphene sheet. The nitrogen atoms used in the graphite plane form a C-N covalent bond in the graphene sheet, thereby changing the electron density of the carbon. The replacement of the edges of carbon atoms by nitrogen atoms also increases vacancies and defects, further improving the electrochemical lithium-ion storage activity of the composite material. In addition, the addition of CNF can form a relatively strong 3D structure, which can not only effectively accommodate and buffer the volume change of silicon but also prevent cracking of the electrode structure and prevent silicon particles from falling off the carbon base due to the expansion of the surface area. CNF is interspersed around Si nanoparticles and graphene to reduce the accumulation of graphene layers and shorten the transmission distance of Li^+ and electrons.

To better understand the chemical reaction kinetics of each sample, the EIS patterns of different electrodes at frequencies ranging from 10 mHZ to 100 kHZ and amplitude ratios of 5 mV were studied (Figure 8(d)). An equivalent circuit for fitting impedance is inserted in in Figure 8(d), where R_e, $R_{SEI,}$ and R_{CT} represent the resistance of ion transport in the electrolyte solution, the resistance of Li^+ migration through the surface membrane, and the resistance of charge transfer. CPE1 and CPE2 correspond to surface film and double-layer capacitors, respectively. We can see that all the curves in the Nyquist plots appear as a semicircle in the high-frequency and middle-frequency regions, and appear as a slanted line in the low-frequency region. The diameter of the semicircle is related to the resistance of lithium ions through the insulating layer on the surface of the active material particles (R_{SEI}) and the charge-transfer resistance (R_{CT}). The slanted line corresponds to the diffusion resistance of lithium ions within the electrode active material. The diffusion resistance is correspondingly expressed as Warburg impedance (Z_W)[24, 47, 49]. As shown in the figure 8(d), the R_{CT} of Si@N-doped rGO/CNF composite material is only 195.0 Ω, which is much lower than Si@N-doped rGO composite material (295.6 Ω) and Si/rGO/CNF composite material (683.5 Ω). This shows that the Si@N-doped rGO/CNF composite material can

 doi:10.20944/preprints202106.0411.v1

effectively promote the conduction of electrons, thereby reducing the charge-transfer resistance and improving the electrochemical performance.

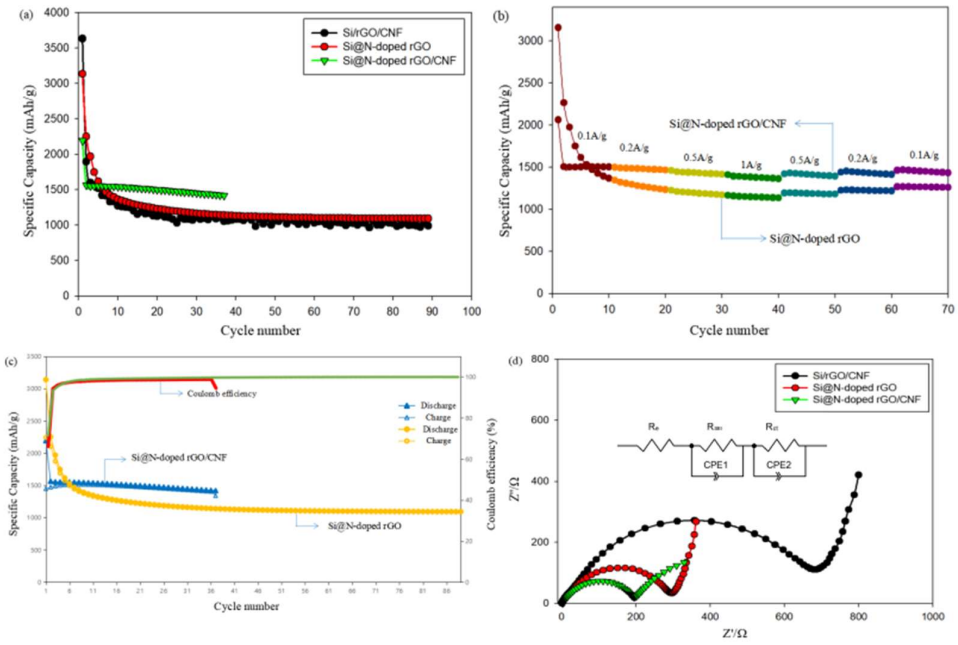

Figure 8. (a) Cycling performances of the synthesized Si/CNF/rGO, Si@N-doped rGO and Si@N-doped rGO/CNF composite electrodes at a current density of 0.1A·g^{-1}, (b) Rate performances of Si@N-doped rGO and Si@N-doped rGO/CNF electrodes under different current densities, (c) Charging and discharging cycle performance and coulomb efficiency of Si@N-doped rGO and Si@N-doped rGO/CNF electrodes, (d) Nyquist plots and electrochemical impedance spectra of the Si/CNF/rGO, Si@N-doped rGO and Si@N-doped rGO/CNF composite electrodes.

4. Conclusion

In this study, we successfully synthesized Si@N-doped rGO/CNF composite electrodes through the electrostatic attraction of amino and carboxyl groups and hydrothermal self-assembly. N-doped rGO is successfully introduced into pyridine N, pyrrole N, and graphite N, which make the graphene structure produce more vacancies and defects. This provides more channels for the transportation of lithium ions and promotes electron transfer during the cycle, thereby improving the conductivity of the electrode. The three-dimensional structure formed by the close combination of Si, N-doped rGO, and CNF, on the one hand, can effectively buffer the volume expansion and contraction of silicon nanoparticles, prevent the silicon nanoparticles from peeling off the graphene sheet, and maintain the stability of the electrode; On the one hand, it effectively prevents the direct contact between the electrolyte and the silicon nanoparticles, thereby forming a stable SEI film. Si@N-doped rGO/CNF electrode has a reversible capacity of 1418.8 mAh/g and a capacity retention rate of 64.7% at a current density of 0.1 A·g^{-1}. The composite electrode has excellent cycle stability and rate performance and provides a reference value for the research of the next generation negative electrode of lithium-ion batteries.

Supplementary Materials: The following are available online, Figure S1. Process for preparing the catalysts and the synthesis of carbon nanofibers. Figure S2. The EDS mapping of the Si, N, C, O elements on the surface of the Si@N-doped rGO/CNF composite. Table S1. Raman spectroscopy results of the GO, rGO, CNFs, Si/rGO, and Si/CNF/rGO samples (see Fig. 4(b)). Table S2. Discharge capacity, coulomb efficiency, and capacity retention rate of the Si/CNF/rGO, Si@N-doped rGO and Si@N-doped rGO/CNF composite electrodes.

Author Contributions: RC wrote the main manuscript text, MJ and HL prepared Figures 7 and 8. All authors reviewed the manuscript.

Funding: This research was supported by the BISA Research Grant of Keimyung University in 2020 (Grant number not available). This research was also supported by the National Research Foundation and Ministry of education of Korea government (project no. NRF-2020R1I1A3060565).

Data Availability Statement: The datasets generated during and/or analyzed during the current study are available from the corresponding author on reasonable request.

Conflicts of Interest: There are no conflicts of interest to declare.

Sample Availability: Samples are not available from the authors.

References

1. Z.L. Xu, J.K. Kim, K. Kang. Carbon nanomaterials for advanced lithium sulfur batteries. Nano Today 2018, 19, 84–107.
2. J. Wang, H. Tang, L. Zhang, H. Ren, R. Yu, Q. Jin, J. Qi, D. Mao, M. Yang, Y. Wang, P. Liu, Y. Zhang, Y. Wen, L. Gu, G. Ma, Z. Su, Z. Tang, H.Zhao,D.Wang. Multishelled metal oxides prepared via an anion-adsorption mechanism for lithium-ion batteries. Nat. Energy 2016, 1, 16050.
3. X. Zhang, E. Qu, Q. Xiao, et al. Preparation of coaxial Sn-Co alloy/CNFs 3D freestanding membrane anode by electrochemical Co-deposition for lithium-ion batteries. Ionics 2019, 25 (12), 5735–5743.
4. Feng K, Li M, Liu W, Kashkooli AG, Xiao X, Cai M et al. Silicon-based anodes for lithium-ion batteries: from fundamentals to practical applications. Small 2018, 14, 1702737.
5. Qiao, H., Duan, A., Wang, T., Liu, P., Wang, D., Pan, H., Wang, H. Investigation on Li2FeSiO4 and Li2FeSiO4/C synthesised through facile solid-state reaction. Materials Technology 2019, 1, 1–7.
6. Zhu G, Gu Y, Wang Y, Qu Q, Zheng H. Neuron like Si-carbon nanotubes composite as a high-rate anode of lithium ion batteries. J Alloys Compd 2019, 787, 928–934
7. Q. Pan, P. Zuo, T. Mu, C. Du, X. Cheng, Y. Ma, Y. Gao, G. Yin. Improved electrochemical performance of micro-sized SiO-based composite anode by prelithiation of stabilized lithium metal powder. J. Power Sources 2017, 347, 170–177.
8. Haruta M, Okubo T, Masuo Y, Yoshida S, Tomita A, Takenaka T et al. Temperature effects on SEI formation and cyclability of Si nanoflake powder anode in the presence of SEI-forming additives. Electrochim Acta 2017, 224, 186–193
9. An, Y., Tian, Y., Wei, C., Jiang, H., Xi, B., Xiong, S., Qian, Y. Scalable and Physical Synthesis of 2D Silicon from Bulk Layered Alloy for Lithium-Ion Batteries and Lithium-Metal Batteries. ACS nano 2019, 13, 13690-13701.

10. Huang, Z. et al. Binder-free graphene/carbon nanotube/silicon hybrid grid as freestanding anode for high capacity lithium ion batteries. Compos. A 2016, 84, 386-392.

11. An, Y., Tian, Y., Wei, H., Xi, B., Xiong, S., Feng, J., & Qian, Y. Porosity- and Graphitization-Controlled Fabrication of Nanoporous Silicon@Carbon for Lithium Storage and Its Conjugation with MXene for Lithium-Metal Anode. Advanced Functional Materials 2020, 30, 1908721.

12. E. Qu, T. Chen, Q. Xiao, et al. Flexible freestanding 3D Si/C composite nanofiber film fabricated using the electrospinning technique for lithium-ion batteries anode. Solid State Ionics 2019, 337, 70–75.

13. K.S. Eom, J.T. Lee, M. Oschatz, F. Wu, S. Kaskel, G. Yushin, T.F. Fuller. A stablelithiated siliconechalcogen battery via synergetic chemical coupling betweensilicon and selenium. Nat. Commun. 2017, 8, 13888.

14. Huang, Y. et al. Porous silicon–graphene–carbon composite as high performance anode material for lithium ion batteries. J. Energy Storage 2020, 27, 101075.

15. Kim, J. M., Ko, D., Oh, J., Lee, J., Hwang, T., Jeon, Y., Piao, Y. Electrochemically exfoliated graphene as a novel microwave susceptor: the ultrafast microwave-assisted synthesis of carbon-coated silicon−graphene film as a lithium-ion battery anode. Nanoscale 2017, 9(40), 15582–15590.

16. X. Wang, L. Lv, Z. Cheng, J. Gao, L. Dong, C. Hu, L. Qu. High-density monolith of N-doped holey graphene for ultrahigh volumetric capacity of Li-ion batteries. Adv. Energy Mater 2016, 6, 1502100.

17. R. Zhou, H. Guo, Y. Yang, Z. Wang, X. Li, Y. Zhou. N-doped carbon layer derived from polydopamine to improve the electrochemical performance of spray-dried Si/graphite composite anode material for lithium ion batteries. J. Alloy. Comp. 2016, 689, 130-137.

18. T. Mu, P. Zuo, S. Lou, Q. Pan, H. Zhang, C. Du, Y. Gao, X. Cheng, Y. Ma, H. Huo, G. Yin. A three-dimensional silicon/nitrogen-doped graphitized carbon composite as high-performance anode material for lithium ion batteries. J. Alloy. Comp. 2019, 777, 190-197.

19. T. Mu, P. Zuo, S. Lou, Q. Pan, Q. Li, C. Du, Y. Gao, X. Cheng, Y. Ma, G. Yin. A two-dimensional nitrogen-rich carbon/silicon composite as high performance anode material for lithium ion batteries. Chem. Eng. J. 2018, 341, 37-46.

20. W.W. Lu Shi, Anbang Wang, Keguo Yuan, Zhaoqing Jin. Si nanoparticles adhering to a nitrogen-rich porous carbon framework and its application as a lithium-ion battery anode material. J. Mater. Chem. 2015, 3, 8.

21. Y. Li, Z. Wang, X.-J. Lv. N-doped TiO2 nanotubes_N-doped graphene nano-sheets composites as high performance anode materials in lithium-ion battery. J. Mater. Chem. 2014, 2, 7.

22. Xu, Y., Sun, X., Wei, C., & Liang, G. Self-assembly by electrostatic attraction to encapsulate Si in N-rich graphene for high performance lithium-ion batteries. Journal of Electroanalytical Chemistry 2020, 867, 114125.

23. X. Li, Y. Bai, M. Wang, G. Wang, Y. Ma, L. Li, B. Xiao and J. Zheng. Self-assembly encapsulation of Si in N-doped reduced graphene oxide as lithium ion battery anode with significantly enhanced electrochemical performance. Sustainable Energy Fuels 2019, 1, 1-37.

24. Na, R., Liu, Y., Wu, Z.-P., Cheng, X., Shan, Z., Zhong, C.-J., & Tian, J. Nano-Silicon composite materials with N-doped graphene of controllable and optimal pyridinic-to-pyrrolic structural ratios for lithium ion battery. Electrochimica Acta 2019, 321, 134742.

25. Zhang, X., Lu, W., Zhou, G., & Li, Q. Understanding the Mechanical and Conductive Properties of Carbon Nanotube Fibers for Smart Electronics. Advanced Materials 2019, 1902028.

26. Li, L., Liu, P., Zhu, K., Wang, J., Tai, G., & Liu, J. Flexible and robust N-doped carbon nanofiber film encapsulating uniformly silica nanoparticles: Free-standing long-life and low-cost electrodes for Li- and Na-Ion batteries. Electrochimica Acta 2017, 235, 79–87.

27. Cheng, Z., Hu, Y., Wu, K., Xing, Y., Pan, P., Jiang, L., … Zhang, X. Si/TiO2/Ti2O3 composite carbon nanofiber by one-step heat treatment with highly enhanced ion/electron diffusion rates for next-generation lithium-ion batteries. Electrochimica Acta 2020, 337, 135789.

28. Tan, Y., Meng, L., Wang, Y., Dong, W., Kong, L., Kang, L., & Ran, F. Negative electrode materials of molybdenum nitride/N-doped carbon nano-fiber via electrospinning method for high-performance supercapacitors. Electrochimica Acta 2018, 277, 41–49.

29. Wang, S., Xia, L., Yu, L., Zhang, L., Wang, H., & Lou, X. W. D. Free-Standing Nitrogen-Doped Carbon Nanofiber Films: Integrated Electrodes for Sodium-Ion Batteries with Ultralong Cycle Life and Superior Rate Capability. Advanced Energy Materials 2015, 6(7), 1502217.

30. Carneiro, O. C., Rodriguez, N. M. & Baker, R. T. K. Growth of carbon nanofibers from the iron–copper catalyzed decomposition of CO/C2H4/H2 mixtures. Carbon 2005, 43, 2389-2396.

31. Cen, Y., Qin, Q., Sisson, R. D., & Liang, J. Effect of Particle Size and Surface Treatment on Si/Graphene Nanocomposite Lithium-Ion Battery Anodes. Electrochimica Acta 2017, 251, 690–698.

32. Meng, K., Guo, H., Wang, Z., Li, X., Su, M., Huang, B., … Peng, W. Self-assembly of porous-graphite/silicon/carbon composites for lithium-ion batteries. Powder Technology 2014, 254, 403–406.

33. Luo, Z., Xiao, Q., Lei, G., Li, Z., & Tang, C. Si nanoparticles/graphene composite membrane for high performance silicon anode in lithium ion batteries. Carbon 2016, 98, 373–380.

34. Mu, T., Zuo, P., Lou, S., Pan, Q., Li, Q., Du, C., Yin, G. A two-dimensional nitrogen-rich carbon/silicon composite as high performance anode material for lithium ion batteries. Chemical Engineering Journal 2018, 341, 37–46.

35. Kikuchi, K., Yamamoto, K., Nomura, N., & Kawasaki, A. Synthesis of n-type Mg2Si/CNT Thermoelectric Nanofibers. Nanoscale Research Letters 2017, 12(1), 1-6.

36. Gao, X., J. Li, Y. Xie, D. Guan, C. Yuan. A Multilayered Silicon-Reduced Graphene Oxide Electrode for High Performance Lithium-Ion Batteries. Acs Applied Materials & Interfaces 2015, 7, 7855.

37. Liu, Z., P. Guo, B. Liu, W. Xie, D. Liu, D. He. Carbon-coated Si nanoparticles/reduced graphene oxide multilayer anchored to nanostructured current collector as lithium-ion battery anode. Applied Surface Science 2017, 396, 41-47.

38. Qin, J., M. Wu, T. Feng, C. Chen, C. Tu, X. Li, C. Duan, D. Xia, D. Wang. High rate capability and long cycling life of graphene-coated silicon composite anodes for lithium ion batteries. Electrochimica Acta 2017, 256, S0013468617320807.

39. Ming-Shan, W., W. Zhi-Qiang, J. Ran, Y. Yi, Z. Fang-Yu, Y. Zhen-Liang, H. Yun, L. Xing, X. Wu. Facile electrostatic self-assembly of silicon/reduced graphene oxide porous composite by silica assist as high performance anode for Li-ion battery. Applied Surface Science 2018, 456, 379-389.

40. Fang, R., Xiao, W., Miao, C., Mei, P., Yan, X., Zhang, Y., & Jiang, Y. Improved lithium storage performance of pomegranate-like Si@NC/rGO composite anodes by facile in-situ nitrogen doped carbon coating and freeze drying processes. Journal of Alloys and Compounds 2020, 834, 155230.

41. Wu, C., Lin, J., Chu, R., Zheng, J., Chen, Y., Zhang, J., & Guo, H. Reduced graphene oxide as a dual-functional enhancer wrapped over silicon/porous carbon nanofibers for high-performance lithium-ion battery anodes. Journal of Materials Science 2017, 52(13), 7984–7996.

42. Yu, L., Liu, J., He, S., Huang, C., Gong, Z., Gan, L., & Long, M. N-doped rGO/C@Si Composites Using Sustainable Chitosan as the Carbon Source for Lithium-Ion Batteries. Applied Surface Science 2020, 501, 144136.

43. C. Sun, Y. Deng, L. Wan, X. Qin, G. Chen, Graphene oxide-immobilized NH2- terminated silicon nanoparticles by cross-linked interactions for highly stable silicon negative electrodes, ACS Appl. Mater. Interfaces 2014, 6, 11277-11285.

44. Zhu, J., Yang, J., Xu, Z., Wang, J., Nuli, Y., Zhuang, X., & Feng, X. Silicon anodes protected by a nitrogen-doped porous carbon shell for high-performance lithium-ion batteries. Nanoscale 2017, 9(25), 8871–8878.

45. Faniyi, I.O., Fasakin, O., Olofinjana, B. et al. The comparative analyses of reduced graphene oxide (RGO) prepared via green, mild and chemical approaches. SN Appl. Sci. 2019, 1, 1181.

46. Gong, Y., Li, D., Fu, Q., & Pan, C. Influence of graphene microstructures on electrochemical performance for supercapacitors. Progress in Natural Science: Materials International 2015, 25(5), 379–385.

47. Rochman, R. A., Wahyuningsih, S., Ramelan, A. H., & Hanif, Q. A. Preparation of nitrogen and sulphur Co-doped reduced graphene oxide (rGO-NS) using N and S heteroatom of thiourea. IOP Conference Series: Materials Science and Engineering 2019, 509, 012119.

48. Johra, F. T., & Jung, W.-G. Hydrothermally reduced graphene oxide as a supercapacitor. Applied Surface Science 2015, 357, 1911–1914.

49. Cong, R., Choi, JY., Song, JB. et al. Characteristics and electrochemical performances of silicon/carbon nanofiber/graphene composite films as anode materials for binder-free lithium-ion batteries. Sci Rep 2021, 11, 1283.

50. Tang, X., Wen, G., Zhang, Y., Wang, D., & Song, Y. Novel silicon nanoparticles with nitrogen-doped carbon shell dispersed in nitrogen-doped graphene and CNTs hybrid electrode for lithium ion battery. Applied Surface Science 2017, 425, 742–749.